



CrossMark
click for updates

Cite this: *RSC Adv.*, 2014, 4, 34315

Visible light-driven decomposition of gaseous benzene on robust Sn²⁺-doped anatase TiO₂ nanoparticles†

Huaqiang Zhuang, Quan Gu, Jinlin Long,* Huan Lin, Huaxiang Lin and Xuxu Wang*

This work shows the efficient degradation of benzene over robust Sn²⁺-doped TiO₂ nanoparticles prepared by a facile sol–gel route under visible light irradiation. The structure, optical properties and chemical states of Sn species incorporated into anatase TiO₂ were carefully characterized by X-ray diffraction, transmission electron microscopy, Raman, UV-vis diffuse reflectance, X-ray photoelectron, X-ray absorption, and electron spin resonance (ESR) spectroscopy. The maximal conversion rate of benzene achieved is up to 27% over the Sn/TiO₂ with a Ti/Sn atomic ratio of 40 : 1 and remains constant for a cyclic run of six days, indicating the high photo-stability for the decomposition of benzene. The characterization results reveal that the Sn²⁺-doping narrows the band gap energy of anatase TiO₂, leading to a visible-light response. The photocatalytic degradation pathway of benzene was proposed based on the results of ESR and Fourier transform infrared spectra. These results offer a full comprehension of the visible light photocatalysis of Sn²⁺-doped TiO₂ for degradation of volatile organic pollutants.

Received 18th June 2014

Accepted 29th July 2014

DOI: 10.1039/c4ra05904b

www.rsc.org/advances

1. Introduction

Benzene is a notorious pollutant released largely from shoe-making, chemical industries, house paints, and so forth. Exposure to the hazardous compound, even at a low level of 1 ppm, increased risk of leukemia and induces some fatal illnesses, such as cancer, teratogenicity, *etc.*^{1,2} The chemical, physical, and biological treatments including catalytic combustion, adsorption, and absorption have been applied widely for removal of benzene from the environment.³ However, these cleanup technologies are inefficient for a ppm concentration of benzene in exhaust gas. Deep removal of benzene and its derivatives is still a formidable challenge for environmental scientists.

Photocatalytic oxidation by light-excited semiconductors has been shown as a promising technology to treat air and water contaminations derived from volatile organic compounds (VOCs), due to its environmental friendly and low cost.^{4–6} Much effort has been devoted to the development of efficient photocatalysts for removal of VOCs. The plenty of inorganic materials including TiO₂, Zn₂GeO₄, β-Ga₂O₃, GaOOH, In(OH)₃, InOOH, ZnSn(OH)₆, Cd₂Sb₂O_{6,8}, and Sr₂Sb₂O₇ have been reported and shown to be photocatalytic active for the oxidation of benzene

under UV light irradiation,^{1,3,7–13} but such photocatalysts were severely restricted in practical application due to several intrinsic drawbacks: (1) the light response of those photocatalysts is limited in UV range of solar spectrum, consequently causing a low quantum efficiency; (2) the photooxidation of benzene exhibits commonly a quick deactivation due to a large amount of carbon deposit on the surface of photocatalysts; (3) a large part of exploited photocatalysts are composed of rare metals, besides TiO₂, and thus greatly increase the use-cost. To broaden the light response into visible light, Li *et al.* prepared a series of nanocomposites by coupling of TiO₂ nanocrystalline with some visible-light responsive vanadates, such as InVO₄, BiVO₄, LaVO₄, and Ag₃VO₄, and showed a promising efficiency for the degradation of benzene under visible light.^{14–17} But the photoactivity of the optimal photocatalyst lasted only for 30–50 hours. The high cost and quick deactivation are two crucial disadvantages for the practical application. Therefore, considering the large-scale application of the photocatalytic technology in environmental purification and remediation, the development of cheap photocatalysts with robust photostability for visible light-driven oxidation of gaseous benzene remains a focus of research in photocatalysis community.

Titanium dioxide (TiO₂) is the most promising photocatalyst for solving current environmental pollution, due to its strong oxidizing ability, high chemical stability, nontoxicity and relatively low cost.¹⁸ Unfortunately, owing to the large band gap of 3.2 eV, it only can be excited by UV light to generate electron–hole pairs.¹⁹ Metal and nonmetal doping has been well-established to be the most simple and effective way to extend its excitation wavelength to visible light.²⁰ Commonly, doping

Research Institute of Photocatalysis, State Key Laboratory of Photocatalysis on Energy and Environment, College of Chemistry, Fuzhou University, Fuzhou 350116, People's Republic of China. E-mail: jllong@fzu.edu.cn; xwang@fzu.edu.cn; Web: <http://chem.fzu.edu.cn/szdw/teacherinfo.aspx?id=40>; Fax: +86-591-83779121; Tel: +86-591-83779121

† Electronic supplementary information (ESI) available. See DOI: 10.1039/c4ra05904b

TiO₂ with nonmetal elements such as F, B, P, N, S, C, and I can create significant absorptions in visible light region by introducing a deep energy level in valence band structure of the semiconductor, attributing to the substitution for lattice oxygen atoms.^{21–27} But the metal doping is a more popular method to prepare photofunctional materials, because it often leads to a red shift of the whole band edge. Among these often-used metal dopants including Cr, Mn, Co, V, In, Fe, Bi, Sn, Ni, Ce, and other rare earth (RE) metals,^{28–34} only Bi was found to be effective for the photocatalytic decomposition of benzene under visible light irradiation.³¹ La-doped anatase TiO₂ was only UV light active for the decomposition.³⁵ Relative to Bi, V, Cr, Co, Mn, and RE, Fe and Sn are two cheaper transitional metals.^{36–39} A number of studies showed that the incorporation of Sn⁴⁺ into anatase TiO₂ significantly enhanced the photocatalytic activity for decoloration of dyes and hydrogen production under UV light.^{40–43} Venkata *et al.*⁴⁴ found that Sn/TiO₂ prepared by using SnCl₂ as a Sn source showed excellent photocatalytic activity for degradation of RhB and cresol under visible light irradiation. Anna *et al.*⁴⁵ suggested that Sn²⁺ species in Sn/TiO₂ contributed mainly to the visible light photocatalysis. A few reports also studied the incorporation of Sn²⁺ into tantalates and niobates.⁴⁶ Recently, we also found that the Sn²⁺ dopant can induce hydrogen production over SnO₂ nanoparticles (NPs) under visible light irradiation.⁴⁷ These works inspired us to exploit the new application of Sn²⁺-doped semiconductor photocatalysts in degradation of VOCs.

In this study, we report the first demonstration of visible-light photocatalytic decomposition of gaseous benzene using relatively cheap Sn-doped anatase TiO₂ nanoparticles. Such materials with different Ti/Sn atomic ratios were prepared by a facile method of using tetrabutyl titanate and SnCl₂ as Ti⁴⁺ and Sn²⁺ sources. The structural, optical, and photocatalytic properties of Sn-doped anatase TiO₂ NPs were systematically characterized by X-ray diffraction (XRD), N₂ physical adsorption, transmission electron microscopy (TEM), X-ray absorption fine structure analysis (XAFS), Raman, X-ray photoelectron (XPS), UV-vis diffuse reflectance (UV-vis DRS), electron spin resonance (ESR), and Fourier transform infrared (FTIR) spectroscopies. The characterization results reveal that Sn species doped into anatase TiO₂ are co-present in the form of Sn²⁺ and Sn⁴⁺. With decreasing Ti/Sn atomic ratios, the absorption band edge of the material appears a significant red-shift, corresponding to the decrease in band gap energy. It was found that the Sn-incorporated TiO₂ photocatalyst can not only work under visible light, but has robust photostability for the photocatalytic decomposition of benzene. It can keep very constant photo-reactivity after a cyclic run of six days. A possible molecular pathway for the visible light photocatalytic decomposition of benzene over Sn-incorporated TiO₂ was proposed based on the ESR and FTIR characterizations.

2. Experimental

2.1 Catalyst preparation

The Sn²⁺-doped TiO₂ NPs were synthesized by a sol-gel route. In the typical preparation, firstly, 4 g tetrabutyl titanate (Ti(OBu)₄)

were uniformly dispersed into 40 mL absolute ethanol by ultrasonication for 5 min, and a certain amount of SnCl₂·2H₂O was added in 40 mL distilled water under vigorous magnetic stirring. Then, the tetrabutyl titanate ethanol solution was added dropwise into the SnCl₂ aqueous solution under vigorously stirring at room temperature and the yellow solid was precipitated. After 1 h of the magnetic stirring, the suspension solution was heated at 90 °C on oil bath for 1 h. Finally, the obtained yellow solid was washed with distilled water and then dried at 100 °C for 12 h. The resultant solid samples were denoted as TS-*x* (where *x* represents the atomic ratio of Ti/Sn, *x* = 100, 60, 50, 40, 30, 20, and 5, respectively). N-doped TiO₂ as a reference sample was synthesized by calcining anatase TiO₂ NPs at 450 °C under dry NH₃ flow 10 h, which was designated as N-TiO₂.

2.2 Catalyst characterization

XRD measurement was taken on a Bruker D8 Advance X-ray diffractometer with Cu K α radiation ($\lambda = 1.5406 \text{ \AA}$). Raman spectra were surveyed with 785 nm excitation at room temperature on a Renishaw Raman microscope. UV-vis DRS spectra were recorded on a Varian Cary 500 Scan UV-vis-NIR spectrometer with BaSO₄ as the reference. The Brunauer–Emmett–Teller (BET) specific surface areas were determined by N₂ adsorption at 77 K on a Micromeritics ASAP 2020. XPS spectra were carried out on a VGESCALAB 250 XPS system with a monochromatized Al K α X-ray sources (15 kV 200 W 500 μm pass energy = 20 eV). All binding energies were referenced to the C 1s peak at 284.6 eV of surface adventitious carbon. HRTEM images were obtained by a JEOL model JEM 2010 EX instrument at an accelerating voltage of 200 kV. XAFS spectra were surveyed at Beamline BL14W1 of Shanghai Synchrotron Radiation Facility (SSRF), with the use of a Si (311) double-crystal monochromator. The FTIR experiments were performed in a special IR cell in conjunction with a vacuum system, and the catalyst powders were first pressed into a self-supporting IR disk (35–40 mg, 18 mm diameter), subsequently the disk was placed in the sample holder that could be moved vertically along a cell tube. Before the FTIR measurement was carried out, the disk was treated under dynamic vacuum (10^{-4} Torr) at 333 K for 2 h. After the disk cooled to room temperature, benzene (10 μL) was introduced into the cell with a syringe *via* the septum. After 30 min of benzene adsorption, the sample disk was then irradiated with a 500 W Xe-arc lamp equipped an UV-cutoff ($\lambda > 420 \text{ nm}$) as the visible light source. During illumination, the infrared spectra of the disk were recorded regularly on a Nicolet 670 FTIR spectrometer with a deuterated triglycine sulfate (DTGS) detector at a resolution of 4 cm^{-1} and 32 scans. ESR spectra were measured using a Bruker model A300 spectrometer with a 500 W Xe-arc lamp equipped with an UV-cutoff ($\lambda > 420 \text{ nm}$) as the visible light source. Typically, the water solution of DMPO was first added to 5 mg catalysts. The DMPO-catalyst mixture was sampled using a capillary tube and placed in an ESR tube for the ESR experiments.

2.3 Photocatalytic activity measurements

The photocatalytic degradation of gaseous benzene was carried out in a fixed-bed photoreactor. The photocatalyst (0.45 g, 60–80

mesh) was loaded in a 2 cm-width, 3 cm-long quartz glass reactor connected to a gas chromatograph (GC, HP6890). The experiment was performed in a closed circulation reaction system and a 500 W Xe arc lamp equipped with a UV cutoff ($\lambda > 420$ nm) was used as the visible light source. Benzene was kept in ice water to maintain the system temperature and diluted in a pure oxygen stream. The flow rate of the reaction system was kept at 20 mL min^{-1} . Meanwhile, the equilibrium concentration of benzene was determined to be 200 ppm and the initial concentration of CO_2 was 0 ppm. The concentration of benzene and CO_2 was determined by an online gas chromatograph equipped with a flame ionization detector, a thermal conductivity detector, and a Porapak R column. Benzene was found to be stable in the catalyst loaded reactor without visible light illumination, and no degradation of benzene was observed when it was illuminated in the absence of catalyst.

3. Results and discussion

3.1 Structural and optical characteristics of the TS-x samples

The XRD patterns of the undoped TiO_2 and Sn-doped TiO_2 samples (denoted as TS-x) with different Ti/Sn atomic ratios are shown in Fig. 1A. For the TS-x samples, they exhibit only diffraction peaks of anatase TiO_2 , and no diffraction peaks assigned to SnO , Sn_2O_3 or SnO_2 are discernable, showing that the incorporation of Sn species doesn't alter the crystalline structure of TiO_2 . The Raman study (Fig. S1,† see ESI) further confirms the conclusion. All of diffraction peaks for the TS-x samples don't shift compared to the undoped TiO_2 , implying that Sn species may be highly dispersed into bulk of anatase TiO_2 or on the surface. In addition, it appears that the diffraction peaks of the TS-x samples are weaker and broader compared to the undoped TiO_2 sample, showing the lower crystallinity and smaller particle size. As seen from Table 1 listing their average particle size, which was calculated using the Scherrer formula, the average particle size of the TS-x samples slightly decreases due to the incorporation of Sn species. N_2 adsorption results (Fig. S2,† see ESI) show that the doping greatly changes pore size distribution and increases BET specific surface area. Therefore, it can be concluded that the Sn incorporation has a considerable influence on crystallinity, particle size, and textural properties of anatase TiO_2 . But these changes don't contribute to their visible-light activity, which will be confirmed later.

The Sn incorporation also greatly changes the optical properties of anatase TiO_2 , as shown in Fig. 1B representing the UV-vis DRS spectra of the TS-x samples and undoped TiO_2 .

The undoped TiO_2 exhibits a band-edge absorption in UV region corresponding to the band-gap energy of 3.2 eV.¹⁹ After doping Sn, the band-edge clearly shifts towards visible light region. As shown in the inset in Fig. 1B, the band gap narrows gradually with increasing Sn content. The TS-5 sample with the highest Sn content displays the lowest band gap energy of ca. 2.95 eV, decreasing by 0.25 eV as compared with the undoped TiO_2 . This is consistent with the results of Sn²⁺-doped $\text{Sn}_2\text{Ta}_2\text{O}_7$, $\text{Sn}_2\text{Nb}_2\text{O}_7$, SnO_2 , TiO_2 , and $\text{Ca}_2\text{Ta}_2\text{O}_7$ reported in literature.^{44,46,47} Thus, it is certain that the visible light response of the

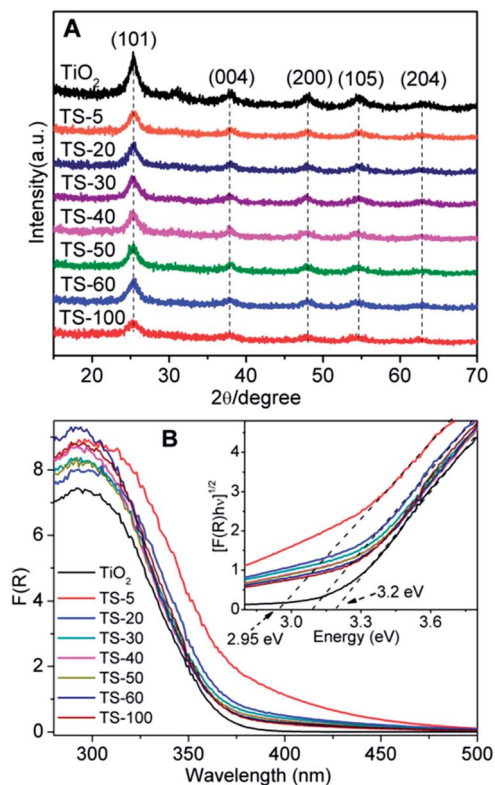


Fig. 1 (A) The XRD patterns of as-prepared TS-x samples and undoped TiO_2 . (B) UV-vis DRS spectra of undoped TiO_2 and TS-x samples. The Insert shows the plots of $[F(R)h\nu]^{1/2}$ vs. photon energy ($h\nu$).

TS-x samples also originates from the Sn^{2+} incorporation, which maybe gives rise to a hybridized group ($\text{Sn}^{2+} 5s\text{-O } 2p$) at the valence band level in the TiO_2 , or the defects formed by the doping.

The morphologies and structural details of the undoped TiO_2 and TS-40 samples are further observed by TEM and HRTEM, as shown in Fig. 2. The Fig. 2A and D show their TEM images, a large quantity of NPs with a diameter of 5–7 nm are discernable, corresponding to the XRD results reported above. The HRTEM images (Fig. 2B and E) display the typical lattice fringes of d -spacing of about 0.35 nm, which is in good agreement with the (101) plane of anatase TiO_2 . Any crystal structures corresponding to metallic Sn and Sn oxides are not observed for the TS-40 sample, but the corresponding EDX pattern confirms the existence of tin as shown by the weak fluorescence signal (Fig. 2F). The EDX mapping spectra (Fig. 2G–J) show homogeneous distribution of Sn, Ti, O elements into the TS-40 sample. These results conclusively indicate that the Sn dopant is highly dispersed into TiO_2 .

3.2 Visible-light photocatalytic activity for benzene photodegradation

The photocatalytic activity of these as-prepared TS-x samples was evaluated by the gas-phase photocatalytic decomposition of benzene under visible light irradiation and compared with that of N-doped TiO_2 (N-TiO_2) as the reference photocatalyst, as

Table 1 The physicochemical characteristics of as-prepared TS-x samples and undoped TiO₂

Entry	TiO ₂	TS-100	TS-60	TS-50	TS-40	TS-30	TS-20	TS-5
Sn content (wt%)	0	1.5	2.5	3.0	3.7	5.0	7.4	29.7
S _{BET} (m ² g ⁻¹)	228.0	255.7	236.8	248.4	248.8	260.7	263.6	257.1
D _A ^b (nm)	6.5	5.9	5.9	5.9	5.6	5.8	5.7	5.4
Ti/Sn ^a (at%)	0	28.6	21.3	20	18.5	13.7	9.3	3.1
Sn ²⁺ /Sn ⁴⁺ (at%)	—	6.4	10.8	10.5	17.9	15.0	11.9	7.6

^a Calculated from the XPS results. ^b The size of anatase particle calculated from the XRD results.

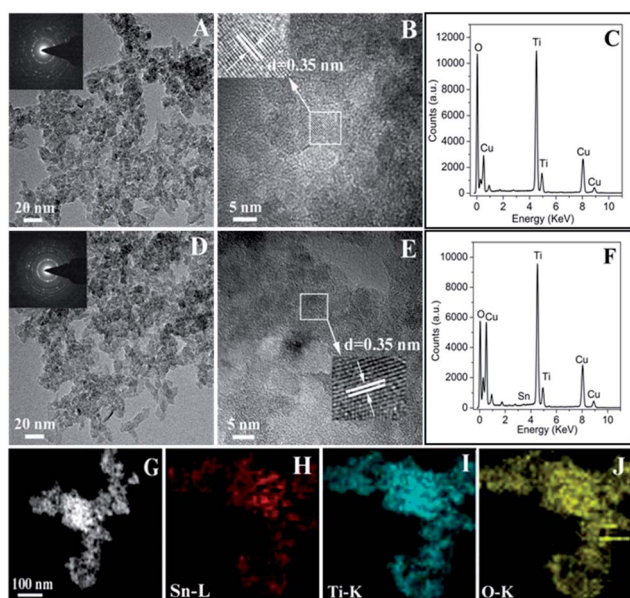


Fig. 2 TEM and HRTEM images of undoped TiO₂ (A and B) and TS-40 (D and E) samples. The figures (C and F) show the EDX patterns of undoped TiO₂ and TS-40 samples, respectively. The Figures (G–J) show the EDX mapping images of Sn, Ti and O elements in the TS-40 sample.

shown in Fig. 3. All of the samples are visible light active for the photocatalytic decomposition of benzene. It appears that upon light on, the conversion rate of benzene quickly rises and reaches a maximum, along with the considerable decrease. All photocatalysts eventually achieve a steady-state conversion of benzene after more than 200 min of light illumination (Fig. 3A), while the mineralization of benzene into CO₂ basically keeps an initial constant (Fig. 3B). More importantly, all of the TS-x samples exhibit a higher conversion of benzene and a higher concentration of produced CO₂, compared to N-TiO₂. It can be seen from Fig. 3C that with decreasing Ti/Sn atomic ratio, the conversion of benzene and the concentration of CO₂ produced increase, and reach a maximum at Ti/Sn atomic ratio of 40, along with the decrease. But the TS-40 sample with the highest conversion of benzene gives a moderate mineralization of about 86%, less than that (92.6%) of the TS-20 sample. Considering this high mineralization, the TS-20 sample was chosen as a representative to further examine the photostability of catalysts for the reaction, which is the most pivotal assessment for the practical application of photocatalysts. As shown in Fig. S3† (see

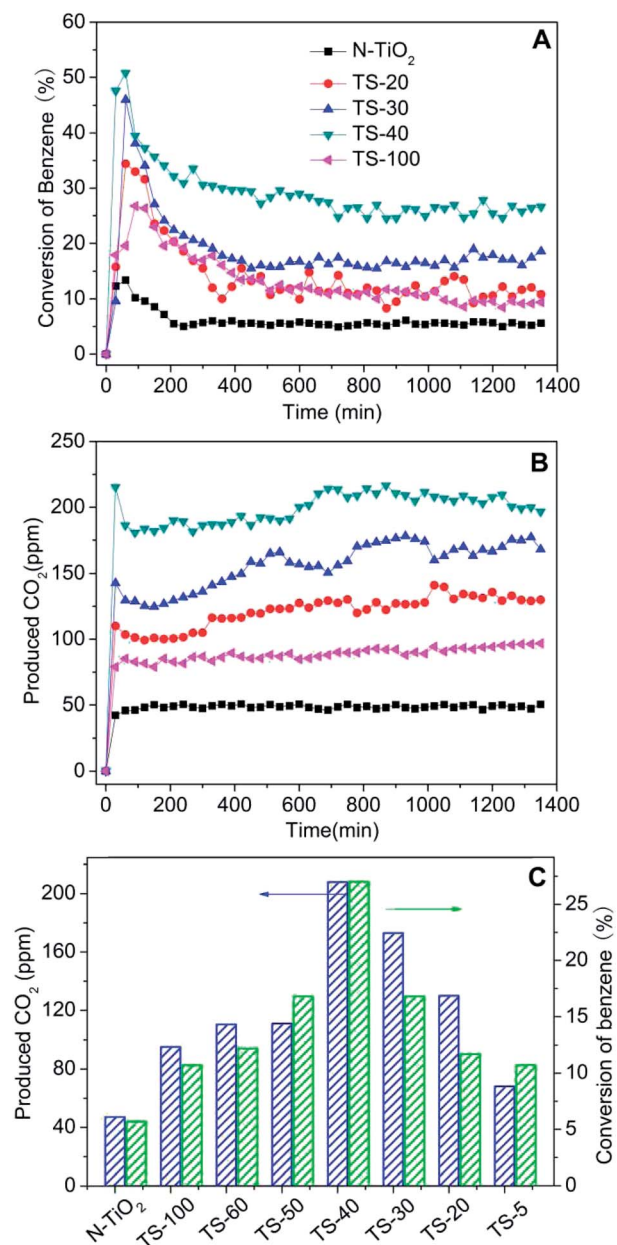


Fig. 3 (A) The conversion of benzene and (B) the yield of produced CO₂ over N-TiO₂, TS-20, TS-30, TS-40 and TS-100 samples, respectively. (C) The change of benzene degradation with different Ti/Sn atomic ratios.

ESI), the catalyst maintains a benzene conversion rate of *ca.* 11.7% and a CO₂ yield of *ca.* 130 ppm during continuously running for 6 days. It is important to note that no obvious deactivation is observed for the catalyst, indicating the promising application in the photocatalytic air purification. Compared to all of the visible light photocatalysts reported so far, the TS-*x* materials are the most robust visible-light photocatalysts for the degradation of benzene.

3.3 Chemical states of Sn species

To reveal the origin of visible-light photocatalysis, XPS was first applied to characterize the chemical states of Sn dopants in TiO₂. Fig. 4 shows the XPS spectra of Ti 2p, O 1s, and Sn 3d for the undoped TiO₂ and TS-*x* samples. The Ti 2p_{3/2} and Ti 2p_{1/2} binding energies locate at 458.5 and 464.3 eV, respectively, which can be attributed to Ti⁴⁺ in TiO₂ (Fig. 4A). The O 1s XPS spectra for all the TS-*x* samples are consisted of two peaks at approximately 530 and 531.6 eV (Fig. 4B). The main peak at *ca.* 530 eV is assigned to the lattice oxygen atoms in TiO₂, and the shoulder at 531.6 eV is attributed to the surface hydroxyls of TiO₂.²⁰ The Sn 3d XPS spectra of the TS-*x* samples (Fig. 4C) can be fitted with four peaks. The set of peaks centered at 485.8 and 494.6 eV belongs to Sn 3d_{5/2} and Sn 3d_{3/2} core levels of Sn²⁺ in tin-oxides doped into TiO₂, and another set of binding energies locating at 486.6 and 495.0 eV is corresponding to Sn⁴⁺ in tin-oxides doped into TiO₂.^{48,49} Moumita *et al.*⁵⁰ also proved the coexistence of Sn²⁺ and Sn⁴⁺ in the Sn-doped TiO₂ materials by

the Mossbauer spectroscopy. After calcination in air, the color of these TS-*x* photocatalysts transforms from yellow into white, losing the visible light absorption. These results further indicate that the visible light response of the as-prepared TS-*x* catalysts results from Sn²⁺ species and defects. It is judged from the intensity of Sn 3d XPS peaks that the Sn²⁺ species are minor in all of the TS-*x* samples, while the Sn⁴⁺ species are predominant. As listed in Table 1, the TS-40 sample gives the largest Sn²⁺/Sn⁴⁺ atomic ratio of 17.9%, corresponding to the highest conversion of atomic ratio as demonstrated in Fig. 4D. The near linear relationship further confirms that the visible light decomposition of benzene is closely related to the Sn²⁺ dopant. Interestingly, the Ti/Sn atomic ratio determined by XPS for all of the TS-*x* samples is far lower than the theoretical value that is calculated by feedstock, conclusively indicating that a majority of Sn species are richened on the surface layer of anatase TiO₂ NPs. This is to say, the Sn species represent a gradient distribution into TiO₂ NPs, gradually decreasing from outside to inside. This result also implies that the surface layer of NPs is the main contributor to the visible light photocatalysis.

The geometric structure of Sn species doped into TiO₂ was further characterized by XAFS. Sn K-edge XAFS data were obtained for SnO, SnO₂, and TS-*x* (*x* = 5, 40, and 60). The XAFS data of SnO and SnO₂ are used as references therein. The normalized Sn K-edge XANES spectra of SnO, SnO₂, TS-5, TS-40, and TS-60 are shown in Fig. 5A. The Sn K-edge positions of TS-5, -40, and -60 are closer to that of the reference SnO₂, instead of SnO, indicating that the majority of tin doped into TiO₂ is present in the form of +4 oxidation state. According to the *E*₀ position (Fig. 5B), it can be concluded that the Sn²⁺ content decreases in the order of TS-40 > TS-5 > TS-60. These results are in line with the XPS results.

The *k*²-weighted Fourier transforms (absolute part) of Sn K-edge EXAFS spectra of the TS-*x* photocatalysts are displayed in Fig. 5C. There is only one maximum between 1.0 and 2.0 Å, which is assigned to the oxygen atoms surrounding the tin absorber in the first shell (without phase correction). Only one weak back-scattering arising from Sn–Sn coordination shell is discernable in the radial distribution function at 2.8 Å, indicating the presence of oligonuclear tin–oxo species. A model consisting of a single tin absorber coordinated to one shell of oxygen atoms and one shell of tin atoms was used to fit the Fourier-filtered EXAFS spectra. The best fits are shown in Fig. S4† (see ESI), and the fit results are given in Table 2. The sum of the O neighbors is approximately 5 for the TS-*x* (*x* = 5, 40, 60) samples. The average Sn–O distance of 2.03 Å in the TS-*x* samples is far lower than that (2.20 Å) of SnO, closer to those (2.04 and 2.05 Å) of SnO₂. Moreover, each tin atom is coordinated, on average, to approximate one tin atom with an average Sn–Sn distance of *ca.* 3.15 Å. Also, the Sn–Sn distance is far lower than the Sn–Sn1 distance (3.52 Å) of SnO, closer to that (3.17 Å) of SnO₂. It can be thus concluded that Sn species present as SnO_{*x*} nanoclusters into TiO₂. Unluckily, the detailed composition of these SnO_{*x*} nanoclusters can't be further clarified due to the intrinsic limitation of the XAFS technique.

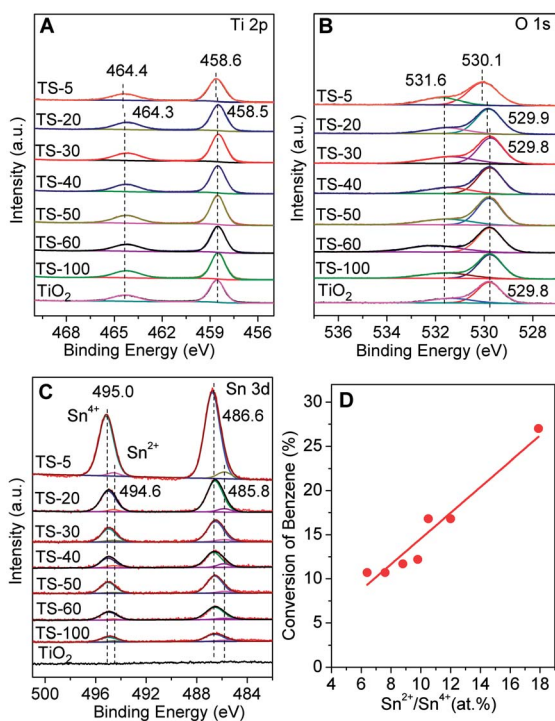


Fig. 4 The high resolution XPS spectra of Ti 2p, O 1s and Sn 3d (A, B and C, respectively) for the undoped TiO₂ and TS-*x* samples. (D) The plot of conversion of benzene vs. Sn²⁺/Sn⁴⁺ atomic ratio for the TS-*x* samples.

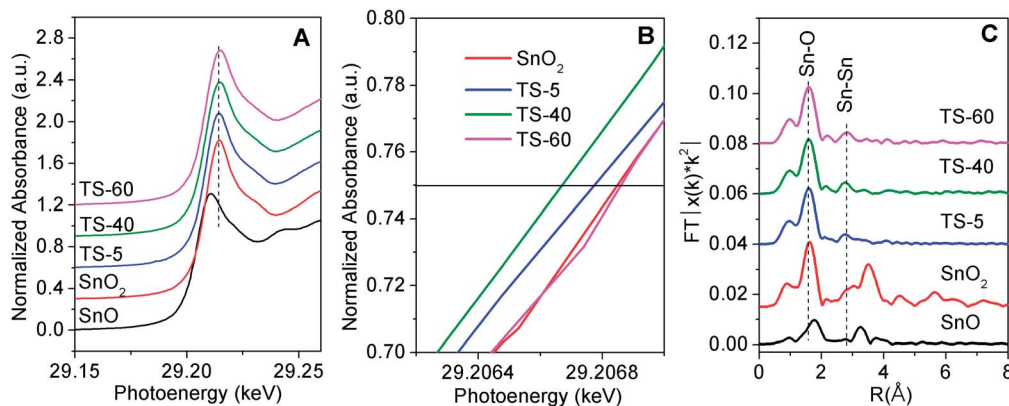


Fig. 5 (A) Normalized Sn K-edge XANES spectra of SnO, SnO₂, TS-5, TS-40 and TS-60 samples. (B) The E_0 positions of SnO₂, TS-5, TS-40 and TS-60 samples in normalized Sn K-edge XANES spectra. (C) Fourier transforms of the Sn K-edge k^2 -weighted EXAFS spectra of the samples.

Table 2 Fit results from EXAFS spectra shown in Fig. 5

Samples	Shell	CN (15%)	R (Å) (10%)	σ^2 (Å ²) (10%)	ΔE_0 (eV) (10%)
SnO ₂	Sn-O1	4.0	2.04	0.0078	13.2
	Sn-O2	2.0	2.05	0.0004	10.7
	Sn-Sn1	2.0	3.17	0.0039	8.4
	Sn-Sn2	4.1	3.73	0.0015	16.8
SnO	Sn-O	4.0	2.20	0.0067	15.6
	Sn-Sn1	4.0	3.52	0.0044	14.9
	Sn-Sn2	4.0	3.66	0.0045	14.8
	Sn-Sn3	4.0	3.80	0.0054	14.5
TS-5	Sn-O	5.2	2.03	0.0050	10.7
	Sn-Sn	0.7	3.15	0.0030	-5.4
TS-40	Sn-O	5.0	2.03	0.0049	11.0
	Sn-Sn	0.8	3.15	0.0041	-5.7
TS-60	Sn-O	5.0	2.03	0.0045	11.4
	Sn-Sn	1.3	3.16	0.0064	-5.2

3.4 ESR study on the visible light photo-excitation of TS-x samples

To further comprehend the visible light-excited mechanism and the probable pathway of electron transfers under visible light irradiation, ESR spectroscopy was employed to survey the TS-x samples at low temperature (100 K). As shown in Fig. 6A, all of the TS-x samples, including the undoped TiO₂, show one weak ESR line at $g = 2.004$. It is definitely attributable to oxygen vacancy created near the surface based on literature.⁵¹ But it is noticeable that after 120 s of visible light irradiation (Fig. 6B), there occur several new ESR signals at $g = 1.998$, 1.988, and 1.958 for all of the TS-x samples. According to literature,⁵²⁻⁵⁴ the set of ESR signals at $g = 1.988$ and 1.958 is unambiguously assigned to surface Ti³⁺ species originated from the electron-trapping of surface-layer Ti⁴⁺ cations, and the line at $g = 1.998$ belongs to a bulk localized defect, such as an electron trapped on a lattice site (F⁺ center), O⁻ species formed by hole-trapping. The $g = 1.998$ line is not observed on the undoped TiO₂ under visible light irradiation, showing that it originates from the Sn doping. The line intensity of surface oxygen

vacancies at $g = 2.004$ is lack of change, indicating that no oxygen vacancies are formed on the surface with visible light irradiation. This is to say, surface oxygen vacancies are not responsible for the visible light excitation, consequently it doesn't contribute to the visible light-driven decomposition of benzene.

The evolution of the F and Ti³⁺ lines with irradiation time was observed for the TS-40 catalyst, as shown in Fig. 6C. Their intensity increases exponentially with the irradiation time, and tends to a plateau after more than 200 s of irradiation. It is noticeable that there is no relationship between the two ESR signals. It can be thus concluded that the electrons trapped on

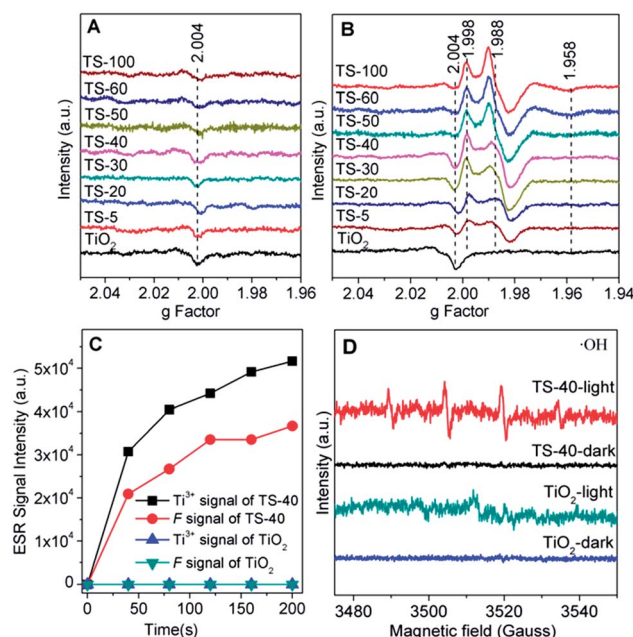
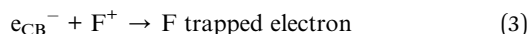
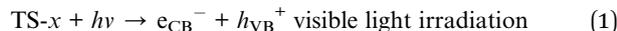


Fig. 6 (A) ESR spectra of the undoped TiO₂ and the TS-x samples without light irradiation. (B) ESR spectra of all samples after 120 s of visible light irradiation at 100 K. (C) The evolution of the F and Ti³⁺ lines with irradiation time under visible light illumination. (D) ESR signals of the DMPO-[•]OH spin adducts for the TS-40 and undoped TiO₂ samples without irradiation and with visible light irradiation.

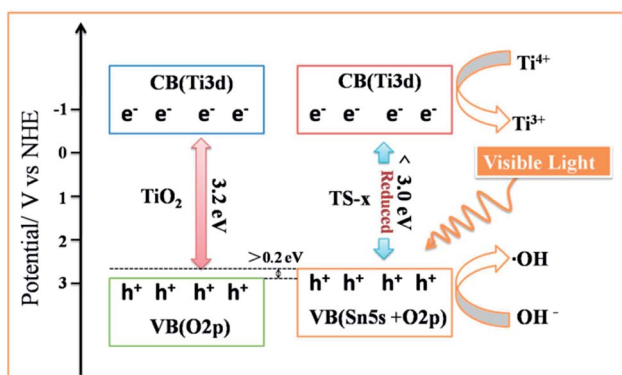
F^+ centers and Ti^{4+} cations as well as the holes trapped by O^{2-} ions should result from the photoexcited Sn^{2+} dopant. The visible light excitation for these TS-x catalysts can be described as follow.



According to the results reported above, the Sn^{2+} species are heterogeneously doped into the bulk of TiO_2 as nanoclusters with a low nuclearity or isolated atoms. The electronic transition for the TS-x catalysts can be regarded as the band-gap transition from the valence band consisting of Sn 5s and O 2p orbitals to the conduction band consisting of Ti 3d orbitals. The Mott-Schottky result shows no any changes in conduction-band structure of Sn^{2+} -doped TiO_2 , which still illuminates the n-type semiconducting feature and the flat-band potential of -0.31 V vs. NHE (Fig. S5,† see ESI). Together with the UV-vis DRS results, it can be concluded that the valence band level of the TS-x catalysts become more negative, relative to that of the pure TiO_2 , because it is controlled by the contribution degree of Sn 5s orbitals as shown in Scheme 1. When the TS-x photocatalysts are illuminated by visible light, the photogenerated electrons are quickly transferred from the Sn^{2+} chromophores to the Ti^{4+} neighbors to form Ti^{3+} species, or to F^+ centers. The photo-generated holes are trapped by nearby lattice oxygen ions to form O^- species, which are capable of oxidizing H_2O to generate hydroxyl radicals.

3.5 Mechanism of visible light-driven decomposition of benzene over TS-x samples

In general, the photocatalytic decomposition of VOCs by semiconductors mainly results from active oxygen species including hydroxyl radicals ($\cdot OH$) and superoxide anion radicals ($O_2^{\cdot -}$), which are produced by the oxidation of water by photo-generated holes and the reduction of O_2 by photogenerated



Scheme 1 Proposed energy diagram for the TS-x material.

electrons, respectively.⁵⁵ The DMPO spin-trapping ESR technique was employed to monitor the formation of these reactive oxygen species, as shown in Fig. 6D. Upon irradiation of the catalyst-water-DMPO suspension with visible light, four characteristic ESR lines belonging to the DMPO- $\cdot OH$ adduct are clearly observed for the TS-40 photocatalyst, while the undoped TiO_2 doesn't appear any ESR signals. It indicates that water can be really oxidized by the irradiated TS-x catalysts to form hydroxyl radicals. Moreover, when the catalyst is dispersed into methanol solution and irradiated with visible light, six weak ESR lines corresponding to the DMPO- $\cdot O_2$ adduct are discernable (Fig. S6,† see ESI), suggesting the smooth transfer of photogenerated electrons from TS-x NPs to adsorbed O_2 . Based on the ESR line intensity of the two adducts, it can be concluded that hydroxyl radicals are the main active species, which play a crucial role in mineralization of benzene into CO_2 and H_2O .

To further clarify the details of the photocatalytic oxidation for benzene, *in situ* FTIR spectroscopy was used to investigate the adsorption and photo-reactivity of benzene on the surface of the optimal catalyst TS-40. Some important intermediates were clearly identified by the technique. Fig. 7 shows the FTIR spectra of the TS-40 surface under benzene atmosphere during visible light irradiation. After heat treatment under dynamic vacuum at 333 K for 2 h, the FTIR spectrum in the region of 1100–2200 cm^{-1} of the TS-40 catalyst exhibits several vibration bands (Fig. 7A-a). The absorption band at 1628 cm^{-1} , corresponding to the bending vibration of water molecules, is the most prominent, indicating that a considerable number of water molecules remain on the catalyst surface. The three bands occurring at 1125, 1071, and 1040 cm^{-1} are corresponding to characteristic absorption peaks for the OR group of titanium tetrabutoxide, which is the precursor of the catalyst.^{56,57} Upon introduction of benzene, there appears a sharp band at 1478 cm^{-1} attributed to the C–C stretching vibration of the aromatic ring and two weak bands at 1825 and 1968 cm^{-1} assigned to the C–H out-of-plane bending vibration of

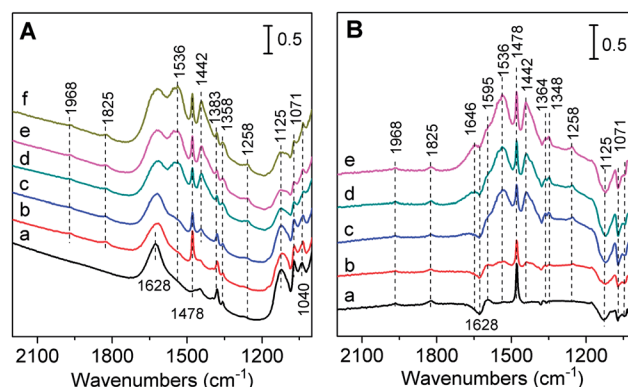
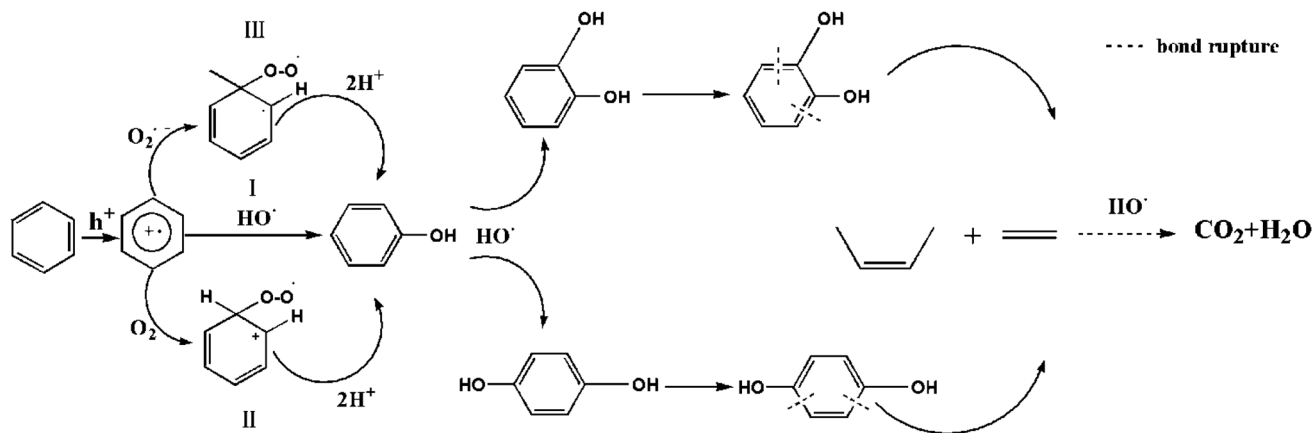


Fig. 7 (A) FTIR spectra of the TS-40 photocatalyst after (a) degassing at 60 °C for 2 h, (b) adsorption of benzene for 30 min at room temperature, and with visible light irradiation for (c) 10, (d) 60, (e) 120 and (f) 180 min. (B) The subtracting FTIR spectra between TS-40 adsorbing benzene and TS-40 sample: (a) adsorption of benzene for 30 min, (b) 10, (c) 60, (d) 120 and (e) 180 min.



Scheme 2 Proposed reaction pathways for photo-oxidation of benzene on TS-x materials.

benzene,^{58,59} indicating that benzene molecules are adsorbed on the catalyst surface (Fig. 7A-b). Visible light irradiation gives rise to tremendous changes in FTIR spectra of the catalyst (Fig. 7A-c-f). Some new bands attributed to products and intermediates appear in the FTIR spectra and increase in intensity with irradiation time. The subtracting spectra between TS-40 adsorbing benzene and TS-40 are able to more clearly illuminate the changes, as shown in Fig. 7B. An intense negative absorbance occurs at 1628 cm^{-1} after adsorbing benzene (Fig. 7B-a), suggesting the substitution of benzene for part of adsorbed water molecules. The six new bands at 1258 , 1348 , 1364 , 1442 , 1536 , 1595 and 1640 cm^{-1} increase in intensity with increasing irradiation time, indicating that they are the products or intermediates arising from the benzene photooxidation. According to literature,⁵⁹⁻⁶¹ the three bands at 1258 , 1364 and 1595 cm^{-1} are consistent with the characteristic peaks of adsorbed phenol, and the three bands at 1348 , 1442 and 1536 cm^{-1} result from the formation of carboxylates on the catalyst surface. The 1640 cm^{-1} band can be attributed to carbonyl-containing adsorbates.⁵⁹ Although these organic molecules containing $-\text{COO}^-$ and $\text{C}=\text{O}$ groups can't be identified completely by the FTIR technique, a possible molecular pathway can be proposed to elucidate the visible light photocatalysis for the decomposition of benzene, together with the previously-reported results by Hisahiro,¹¹ Thuan,^{62,63} and Zhong.⁶⁴ As demonstrated in Scheme 2, the photooxidation of benzene mainly involves the oxygen and hole transfers from catalyst to reactive substrates.⁶⁵⁻⁶⁷ The incorporated Sn^{2+} species can be excited with visible light to produce electron-hole pairs. Electrons are efficiently captured by Ti^{4+} species to form the Ti^{3+} species, which reduce O_2 to $\text{O}_2^{\cdot-}$. Holes not only react with the adsorbed benzene to generate the benzene radical cation ($\text{C}_6\text{H}_5^{\cdot+}$), but also oxidize directly the adsorbed water molecules to form $\cdot\text{OH}$.⁶⁸ There are three possible pathways to produce the phenol intermediates from the $\text{C}_6\text{H}_5^{\cdot+}$. The first one should be the reaction of $\text{O}_2^{\cdot-}$ or O_2 with $\text{C}_6\text{H}_5^{\cdot+}$ to form a peroxide, which can be further converted to phenol by reductive processes (denoted as process I and II, respectively).^{62,63} Another pathway is the direct reaction of hydroxyl radicals ($\cdot\text{OH}$) with $\text{C}_6\text{H}_5^{\cdot+}$ to generate phenol, which is

ultimately oxidized to CO_2 and H_2O via a series of the involvement of hydroxyl radicals. According to the ESR results-reported above that the TS-40 catalyst represents weak ESR signals belonging to superoxide anion radicals, Process I is certainly minor in the visible-light-driven decomposition of benzene over robust Sn^{2+} -doped TiO_2 catalysts. It was more reasonable to suggest that the crucial intermediate, phenol, comes predominantly from process II and the reaction of O_2 molecules with $\text{C}_6\text{H}_5^{\cdot+}$, because the control experiment proves that the presence of O_2 molecules is obligatory for the photocatalytic decomposition of gaseous benzene. This may be the main origin of high photostability for the benzene photooxidation over the TS-x materials, which needs be further studied.

4. Conclusions

In this work, we first demonstrate that the Sn^{2+} -doped TiO_2 nanoparticles are excellent and promising photocatalysts for the visible-light-driven decomposition of benzene with high photostability. An optimal Ti/Sn atom ratio is achieved to be 40 : 1 for the photocatalyst. The detailed characterizations reveal that the Sn^{2+} dopant presents as SnO_x nanoclusters with a low nuclearity. The doping doesn't affect the conduction-band structure of anatase TiO_2 , but introduces a hybridized group ($\text{Sn}^{2+} 5s-\text{O} 2p$) at the valence band level of anatase TiO_2 , consequently the considerable decrease in optical band gap of the TS-x materials. The products and intermediates are well-identified by *in situ* FTIR and ESR spectroscopies, and show some important information on the photooxidation process. The involvement of hydroxyl radicals formed by the hole-oxidation of water should be the main origin of photocatalytic decomposition of benzene under visible light.

Acknowledgements

This work was financially supported by the NSFC (Grants no. 21373051 and U1305242), the Science and Technology project of the Education Office of Fujian Province of P. R. China (JA12017), and National Basic Research Program of China (973 Program,

no. 2012CB722607). We thank Professor Yuying Huang and Professor Zheng Jiang (SSRF) for the XAFS experiments.

References

- 1 X. Fu, X. Wang, Z. Ding, D. Y. C. Leung, Z. Zhang, J. Long, W. Zhang, Z. Li and X. Fu, *Appl. Catal., B*, 2009, **91**, 67–72.
- 2 T. Yan, J. Long, Y. Chen, X. Wang, D. Li and X. Fu, *C. R. Chim.*, 2008, **11**, 101–106.
- 3 T. Yan, J. Long, X. Shi, D. Wang, Z. Li and X. Wang, *Environ. Sci. Technol.*, 2010, **44**, 1380–1385.
- 4 M. R. Hoffmann, S. T. Martin, W. Choi and D. W. Bahnemann, *Chem. Rev.*, 1995, **95**, 69–96.
- 5 Y. Kuwahara and H. Yamashita, *J. Mater. Chem.*, 2011, **21**, 2407–2416.
- 6 X. Z. Li, H. Liu, L. F. Cheng and H. J. Tong, *Environ. Sci. Technol.*, 2003, **37**, 3989–3994.
- 7 Y. Hou, X. Wang, L. Wu, Z. Ding and X. Fu, *Environ. Sci. Technol.*, 2006, **40**, 5799–5803.
- 8 Z. Li, Z. Xie, Y. Zhang, L. Wu, X. Wang and X. Fu, *J. Phys. Chem. C*, 2007, **111**, 18348–18352.
- 9 M. Sun, D. Li, W. Zhang, Z. Chen, H. Huang, W. Li, Y. He and X. Fu, *J. Phys. Chem. C*, 2009, **113**, 14916–14921.
- 10 H. Xue, Z. Li, L. Wu, Z. Ding, X. Wang and X. Fu, *J. Phys. Chem. C*, 2008, **112**, 5850–5855.
- 11 H. Einaga, S. Futamura and T. Ibusuki, *Phys. Chem. Chem. Phys.*, 1999, **1**, 4903–4908.
- 12 J. Huang, X. Wang, Y. Hou, X. Chen, L. Wu and X. Fu, *Environ. Sci. Technol.*, 2008, **42**, 7387–7391.
- 13 M. Sun, D. Li, W. Zhang, X. Fu, Y. Shao, W. Li, G. Xiao and Y. He, *Nanotechnology*, 2010, **21**, 355601.
- 14 G. Xiao, X. Wang, D. Li and X. Fu, *J. Photochem. Photobiol., A*, 2008, **193**, 213–221.
- 15 Y. Hu, D. Li, Y. Zheng, W. Chen, Y. He, Y. Shao, X. Fu and G. Xiao, *Appl. Catal., B*, 2011, **104**, 30–36.
- 16 H. Huang, D. Li, Q. Lin, W. Zhang, Y. Shao, Y. Chen, M. Sun and X. Fu, *Environ. Sci. Technol.*, 2009, **43**, 4164–4168.
- 17 J. Wang, H. Ruan, W. Li, D. Li, Y. Hu, J. Chen, Y. Shao and Y. Zheng, *J. Phys. Chem. C*, 2012, **116**, 13935–13943.
- 18 S. Hoang, S. P. Berglund, N. T. Hahn, A. J. Bard and C. B. Mullins, *J. Am. Chem. Soc.*, 2012, **134**, 3659–3662.
- 19 J. Wang, D. N. Tafen, J. P. Lewis, Z. Hong, A. Manivannan, M. Zhi, M. Li and N. Wu, *J. Am. Chem. Soc.*, 2009, **131**, 12290–12297.
- 20 Z. Zhang, X. Wang, J. Long, Q. Gu, Z. Ding and X. Fu, *J. Catal.*, 2010, **276**, 201–214.
- 21 W. Ho, J. C. Yu and S. Lee, *Chem. Commun.*, 2006, 1115–1117.
- 22 W. Zhao, W. Ma, C. Chen, J. Zhao and Z. Shuai, *J. Am. Chem. Soc.*, 2004, **126**, 4782–4783.
- 23 K. Yang, Y. Dai and B. Huang, *J. Phys. Chem. C*, 2007, **111**, 18985–18994.
- 24 R. Asahi, T. Morikawa, T. Ohwaki, K. Aoki and Y. Taga, *Science*, 2001, **293**, 269–271.
- 25 J. C. Yu, W. Ho, J. Yu, H. Yip, P. K. Wong and J. Zhao, *Environ. Sci. Technol.*, 2005, **39**, 1175–1179.
- 26 J. Yu, G. Dai, Q. Xiang and M. Jaroniec, *J. Mater. Chem.*, 2011, **21**, 1049–1057.
- 27 X. Hong, Z. Wang, W. Cai, F. Lu, J. Zhang, Y. Yang, N. Ma and Y. Liu, *Chem. Mater.*, 2005, **17**, 1548–1552.
- 28 R. Dholam, N. Patel, M. Adami and A. Miotello, *Int. J. Hydrogen Energy*, 2009, **34**, 5337–5346.
- 29 S. Klosek and D. Raftery, *J. Phys. Chem. B*, 2001, **105**, 2815–2819.
- 30 D. Dvoranová, V. Brezová, M. Mazúr and M. A. Malati, *Appl. Catal., B*, 2002, **37**, 91–105.
- 31 Y. Hu, Y. Cao, P. Wang, D. Li, W. Chen, Y. He, X. Fu, Y. Shao and Y. Zheng, *Appl. Catal., B*, 2012, **125**, 294–303.
- 32 A. M. T. Silva, C. G. Silva, G. Dražić and J. L. Faria, *Catal. Today*, 2009, **144**, 13–18.
- 33 D. Hyun Kim, K. Sub Lee, Y.-S. Kim, Y.-C. Chung and S.-J. Kim, *J. Am. Ceram. Soc.*, 2006, **89**, 515–518.
- 34 E. Wang, W. Yang and Y. Cao, *J. Phys. Chem. C*, 2009, **113**, 20912–20917.
- 35 S. Zhang, Z. Zheng, J. Wang and J. Chen, *Chemosphere*, 2006, **65**, 2282–2288.
- 36 E. Arpaç, F. Sayılkan, M. Asiltürk, P. Tatar, N. Kiraz and H. Sayılkan, *J. Hazard. Mater.*, 2007, **140**, 69–74.
- 37 Y. Zhao, J. Liu, L. Shi, S. Yuan, J. Fang, Z. Wang and M. Zhang, *Appl. Catal., B*, 2010, **100**, 68–76.
- 38 H. Yu, H. Irie, Y. Shimodaira, Y. Hosogi, Y. Kuroda, M. Miyauchi and K. Hashimoto, *J. Phys. Chem. C*, 2010, **114**, 16481–16487.
- 39 S. George, S. Pokhrel, Z. Ji, B. L. Henderson, T. Xia, L. Li, J. I. Zink, A. E. Nel and L. Mädler, *J. Am. Chem. Soc.*, 2011, **133**, 11270–11278.
- 40 Y. Zhao, J. Liu, L. Shi, S. Yuan, J. Fang, Z. Wang and M. Zhang, *Appl. Catal., B*, 2011, **103**, 436–443.
- 41 J. Chattopadhyay, H. Rok Kim, S. Bong Moon and D. Pak, *Int. J. Hydrogen Energy*, 2008, **33**, 3270–3280.
- 42 Q. Gu, J. Long, Y. Zhou, R. Yuan, H. Lin and X. Wang, *J. Catal.*, 2012, **289**, 88–99.
- 43 Q. Gu, J. Long, L. Fan, L. Chen, L. Zhao, H. Lin and X. Wang, *J. Catal.*, 2013, **303**, 141–155.
- 44 V. B. R. Boppana and R. F. Lobo, *J. Catal.*, 2011, **281**, 156–168.
- 45 A. Iwaszuk and M. Nolan, *J. Mater. Chem. A*, 2013, **1**, 6670–6677.
- 46 Y. Hosogi, Y. Shimodaira, H. Kato, H. Kobayashi and A. Kudo, *Chem. Mater.*, 2008, **20**, 1299–1307.
- 47 J. Long, W. Xue, X. Xie, Q. Gu, Y. Zhou, Y. Chi, W. Chen, Z. Ding and X. Wang, *Catal. Commun.*, 2011, **16**, 215–219.
- 48 W.-Y. Wu, Y.-M. Chang and J.-M. Ting, *Cryst. Growth Des.*, 2010, **10**, 1646–1651.
- 49 Y. Cao, T. He, L. Zhao, E. Wang, W. Yang and Y. Cao, *J. Phys. Chem. C*, 2009, **113**, 18121–18124.
- 50 M. Ghosh, V. Pralong, A. Wattiaux, A. W. Sleight and M. A. Subramanian, *Chem. – Asian J.*, 2009, **4**, 881–885.
- 51 N. Siedl, S. O. Baumann, M. J. Elser and O. Diwald, *J. Phys. Chem. C*, 2012, **116**, 22967–22973.
- 52 T. Berger, M. Sterrer, O. Diwald, E. Knözinger, D. Panayotov, T. L. Thompson and J. T. Yates, *J. Phys. Chem. B*, 2005, **109**, 6061–6068.
- 53 T. M. Breault and B. M. Bartlett, *J. Phys. Chem. C*, 2012, **116**, 5986–5994.

- 54 E. A. Reyes-Garcia, Y. Sun, K. R. Reyes-Gil and D. Raftery, *Solid State Nucl. Magn. Reson.*, 2009, **35**, 74–81.
- 55 M. Pelaez, N. T. Nolan, S. C. Pillai, M. K. Seery, P. Falaras, A. G. Kontos, P. S. M. Dunlop, J. W. J. Hamilton, J. A. Byrne, K. O'Shea, M. H. Entezari and D. D. Dionysiou, *Appl. Catal., B*, 2012, **125**, 331–349.
- 56 M. Burgos and M. Langlet, *J. Sol-Gel Sci. Technol.*, 1999, **16**, 267–276.
- 57 D. Zare-Hosseini-abadi, A. Ershad-Langroudi, A. Rahimi and S. Afsar, *J. Inorg. Organomet. Polym. Mater.*, 2010, **20**, 250–257.
- 58 M. Nagao and Y. Suda, *Langmuir*, 1989, **5**, 42–47.
- 59 W.-C. Wu, L.-F. Liao, C.-F. Lien and J.-L. Lin, *Phys. Chem. Chem. Phys.*, 2001, **3**, 4456–4461.
- 60 S. Horikoshi, T. Miura, M. Kajitani, H. Hidaka and N. Serpone, *J. Photochem. Photobiol., A*, 2008, **194**, 189–199.
- 61 M. D. Hernández-Alonso, I. Tejedor-Tejedor, J. M. Coronado, M. A. Anderson and J. Soria, *Catal. Today*, 2009, **143**, 364–373.
- 62 T. D. Bui, A. Kimura, S. Ikeda and M. Matsumura, *J. Am. Chem. Soc.*, 2010, **132**, 8453–8458.
- 63 T. D. Bui, A. Kimura, S. Higashida, S. Ikeda and M. Matsumura, *Appl. Catal., B*, 2011, **107**, 119–127.
- 64 J. Zhong, J. Wang, L. Tao, M. Gong, L. Zhimin and Y. Chen, *J. Hazard. Mater.*, 2007, **139**, 323–331.
- 65 G. Palmisano, V. Augugliaro, M. Pagliaro and L. Palmisano, *Chem. Commun.*, 2007, 3425–3437.
- 66 F. Soana, M. Sturini, L. Cermenati and A. Albini, *Perkin 2*, 2000, 699–704.
- 67 H. Park and W. Choi, *Catal. Today*, 2005, **101**, 291–297.
- 68 H. Einaga, T. Ibusuki and S. Futamura, *J. Sol. Energy Eng.*, 2004, **126**, 789–793.